Prediction of Knock Propensity Using Stochastic Modeling in a Spark-Ignition Engine

Seokwon Cho, Chiheon Song, Youngbok Lee , Namho Kim, Sechul Oh and Kyoungdoug Min*

Department of Mechanical Engineering, Seoul National University, Seoul 08826, South Korea

Abstract

To comply with stringent CO2 regulations, enhanced thermal efficiency has been prioritized in internal combustion engine development; however, this has strongly driven the development of engines with operating conditions more prone to knock. Current knock sensors have its limitations to decompose knock signal by degradation so that it required a cross-referencing signal. In addition, knock control intervention is currently preceded by the occurrence of the knock, leading to decrease in thermal efficiency by retarding spark timing.

In the present work, a novel prediction model for knock propensity (incidence) is presented, aiming to enable active control of knock or autoignition, and to support conventional knock sensor for cross-referencing by facilitating virtual knock sensor. A zero-dimensional model-based prediction of the in-cylinder pressure is demonstrated to prevent using in-cylinder pressure transducer, along with other incorporated predictive sub-models for the residual gas fraction, heat loss, burn duration, and heat release rate. Ignition delay correlation and Livengood-Wu relation are used to predict the onset of knock, and a burn point-based criterion is newly proposed for application in stochastic

*Corresponding Author

Kyoungdoug Min, Ph.D., Professor
Department of Mechanical Engineering, Seoul National University, Seoul 08826, Korea
e-mail: kdmin@snu.ac.kr

modeling for determining the knock propensity. The predicted knock propensity from the combined holistic model shows a remarkable agreement with experimental results.

Keywords (6)

Knock, ignition delay, autoignition, stochastic model, zero-dimensional model, prediction

Abbreviations

0D	zero-dimensional
1D	one-dimensional
aBDC	after bottom dead center
ANN	artificial neural network
ASTM	American Society for Testing and Materials
aTDC	after top dead center
bBDC	before bottom dead center
BDC	bottom dead center
bTDC	before top dead center
CA	crank angle
CA50	crank angle at MFB50
CA90	crank angle at MFB90
CR	compression ratio
CVVT	continuous variable valve timing
ECU	engine control unit
EGR	exhaust gas recirculation
EMS	engine management system
EVC	exhaust valve closing
EVO	exhaust valve opening
IVC	intake valve closing
IVO	intake valve opening
KO	knock onset
LHV	lower heating value
MAP	manifold absolute pressure
MFB	mass fraction burned
nIMEP	net indicated mean effective pressure
OF	overlap factor
RGF	residual gas fraction
RMSE	root mean square error
RON	research octane number
SI	spark-ignition
TDC	top dead center
VO	valve overlap
WOT	wide open throttle

1. Introduction

Recently, as global regulations for fuel economy and harmful emissions have become increasingly stringent, a substantial focus has been given to the research and development of engines with higher efficiency. In a spark-ignition (SI) engine, one of the critical approaches to increasing the fuel conversion efficiency is to increase the compression ratio, as the compression ratio has a direct relationship with the theoretical efficiency [1].

However, increasing the compression ratio is generally limited by the occurrence of knock. This is because knock is caused by end-gas autoignition, which occurs at high pressures and temperatures, and a higher compression ratio increases the peak pressure and temperature. Knock is generally accompanied by undesirable noise and damage (if severe) to the engine; therefore, it must be suppressed [2, 3].

A knock sensor mounted on an engine block detects the vibration caused by the pressure oscillation transmitted from an acoustic knock in the combustion chamber. In the production engine, detecting knock by filtering knock sensor's signal, e.g., applying cut-off frequency with a band-pass filter, has a limitation, although it is reliable and the most cost-effective solution. Signal achieved from knock sensor is extremely sensitive to noise and frequency [4], so that the signal is easily attenuated by other disturbances such as a change in engine speed [2, 5]. Because the noise level of other vehicle components substantially increases, engine control needs to rely on a higher oscillation-mode signal of the sensor, leading to a low signal-to-noise ratio. Higher oscillation modes were also reported with lower signal intensity [6-8]. Therefore, reference information of knock propensity provided by model-based prediction can significantly improve the sensor's reliability.

As vehicle mileage increases, degradation of vehicle parts is inevitable so that noise interference to knock sensor becomes exacerbated. Therefore, adaptation logic that adjusts the knock threshold by the time is being applied in the field. However, it is difficult to expect the adaptive threshold is pertinent, and this also can cause a sensor reliability issue. Therefore, having a reference input can be very advantageous in this perspective.

The cross-referencing of the signal would also be beneficial in terms of on-board diagnostics of knock sensor failure. The on-board diagnostics technique becomes crucial for engine production because not only the emission regulations are getting substantially stringent [9] but also it has been an efficient solution to keep good conditions of vehicle and its powertrain. As failure or malfunction of knock sensor can cause severe engine damage and/or deteriorate the efficiency, cross-referencing with model-based input can help the system better evaluate the sensor status.

The compression ratio is fixed for a given engine design unless a variable compression ratio system is utilized. Thus, knock can be suppressed by using a high-octane rating fuel, and can be practically avoided by moderately retarding the spark timing during engine operation [1-3]. However, overly retarded spark timing from the optimum (e.g., the maximum brake torque) reduces the engine's thermal efficiency by causing an excessive exhaust heat loss; therefore, appropriate control spark timing is required to maintain high efficiency.

Typical modern engines use passive control for knock suppression [10]: the engine control unit (ECU) retards the spark timing when it detects knock. Although this type of knock control is instantaneous and promising for knock mitigation, certain limitations still exist. The spark timing control engages after the occurrence of knock [11, 12]; consequently, undesirable vibrations and noise are delivered to the driver before the control is activated. The production cost of the engine slightly increases, owing to the installation of the knock sensor. Finally, there is an additional loss in thermal efficiency from running the engine overly retarded spark timing (relative to the optimal value). To overcome the above limitations, active control of the spark timing can be beneficial by forecasting the probability of knock occurrence, and to predetermine a pertinent spark timing. By introducing active spark timing control, the efficiency loss can be minimized.

Because knock stems from the autoignition of the end gas, the occurrence of knock can be predicted to some degree by calculating the ignition delay of a given reactant. Assuming a one-step reaction mechanism, the ignition

delay time can be described using the Arrhenius equation. The first attempt to estimate the autoignition timing using a zero-dimensional (0D) model was made by Livengood and Wu [13]. Assuming that the autoignition reaction is zero-order and the reaction rate constants do not change, the relationship between the concentration and ignition delay can be expressed as shown in Eq. 1, where τ is the ignition delay, and $(x)/(xc)$ is the concentration ratio of mixture. It is considered that autoignition occurs when the right-hand side of Eq. 1 reaches unity.

$$\frac{x}{x_c} = \int_{t=0}^{t=t_e} \frac{1}{\tau} dt \quad \text{(Eq.1)}$$

The ignition delay (τ) under certain conditions can be estimated using computational methods, e.g., by using 0D empirical correlations [13-23] or solving detailed chemical mechanisms [24-27]. For real-time control during engine operation, the 0D empirical correlation must be used to minimize the computation time.

Numerous predictive knock models have been developed based on 0D empirical ignition delay correlations [13-23]. Two-stage ignition delay correlations [28-30] have also been suggested to improve the prediction by applying the negative temperature coefficient behavior of the fuels. However, previous models have exclusively relied on the measured in-cylinder pressure, thereby incurring additional production costs. In addition, a calculation based on the measured in-cylinder pressure cannot realistically be a predictive model. In this perspective, prediction of in-cylinder pressure is necessary.

To employ a model to the engine control unit, it is necessary to have a fast calculation speed for such prediction. Several studies reported 0D-based fast prediction of in-cylinder pressure is feasible in a diesel engine [31-33] , and the studies showed a successful development of virtual NOx sensor by calculating empirical sub-models based on the predicted in-cylinder pressure. Li et al. [34] recently reported a predictive knock model using a two-zone-based combustion model in a spark-ignition engine and proposed a feedforward stochastic knock limit control [35] thereafter. The study suggested 0D-based prediction of in-cylinder pressure, which can secure the fast calculation speed, and

the model introduced a two-step chemical reaction mechanism to predict the combustion process. A great performance of knock control was shown using the developed combustion model, although the engine operating points were limited, and thermodynamic condition at intake valve closing was fixed where it is fully variable depending on engine operating condition.

For above all reasons, this study suggests predictive model for in-cylinder pressure and knock propensity that can possibly be adopted in engine management system (EMS) in the future. There is a need for a model that can provide an accurate estimation of knock propensity based on the predicted in-cylinder pressure, i.e., to deploy moderate spark timing for an engine, maximize the engine running efficiency, and support or replace the knock sensor. The modeling should be restricted to use parameters that only available from the EMS for its applicability and to prevent cost increase by additional sensor application. In addition, a great number of modern gasoline engines utilizes variable valve system to increase the thermal efficiency by varying the valve timings so that the model has to be able to cover the change coming from such variations. In addition, the Livengood-Wu integral method does not represent the strength of the knock, i.e., the knock intensity or magnitude. Therefore, a method for predicting the knock propensity (not timing) is proposed.

This study consists of three main aspects: the engine experimental setup, model development for in-cylinder pressure and knock prediction, and stochastic modeling for predicting the knock propensity. The limitations and future works are also given at the end.

2. Experimental setup and conditions

2.1 Experimental setup

The experiments were conducted using a single-cylinder port fuel injection engine. The engine had a displacement volume of 0.5 L, and the bore and stroke were 81 mm and 97 mm, respectively. The geometric compression ratio was 12. The other engine specifications, including the valve timings, are listed in Table 1.

Table 1. Test engine specifications

Displacement volume [cc]	499.8
Bore [mm]	81
Stroke [mm]	97
Conrod length [mm]	150.9
Piston offset [mm]	10.4
Exhaust valve opening (EVO)/ Exhaust valve closing (EVC)	71 CA bTDC / 5 CA aTDC
Intake valve opening (IVO)[1]/ Intake valve closing (IVC)[1]	5 CA aTDC / 62 CA aBDC
Compression ratio	12
Injection system	Dual port fuel injection (3.5 bar)
Injection timing	540 CA bTDC
Number of valves	4
Maximum valve lift [mm]	10

[1]Parking position

Fig. 1 shows a schematic diagram of the experimental setup. The in-cylinder pressure was measured using a Kistler 6056A piezoelectric pressure transducer, and the sensor was flush-mounted in the cylinder head. The acquired raw in-cylinder pressure signal was amplified by an AVL IFEM. The intake manifold pressure was measured using a Kistler 4045A5 sensor, and the signal was amplified using a Kistler 4603 amplifier. Both the intake and in-cylinder pressure signals were acquired with an AVL Indimodule with 0.1 crank angle (CA) resolution, and Indicom 2.0 software was used to log the pressure data. At least 2,000 consecutive engine cycle data was achieved for high repeatability of the experiment as well as for statistical approach for knock analysis that will be presented in knock metric section. A Horiba MEXA-7100 DEGR gas analyzer was used to monitor emissions

during the experiment, and a Horiba MEXA-110λ analyzer was used to monitor the air excess ratio. An OVAL CA001 Coriolis fuel flowmeter was used to measure the fuel flow rate by averaging a 1 Hz signal for three minutes. A continuous variable valve timing (CVVT) module for varying the intake valve timing was controlled with an ECU using the ETAS INCA software. For repeatable control of the valve timing, the actual cam position was monitored when adjusting the cam phasing. Market gasoline fuel was used in this study, and the properties are shown in Table 2. The fuel had a research octane number of 91.5 and low heating value of 42.8 MJ/kg. The number of oxygenate originates from the additives in the fuel.

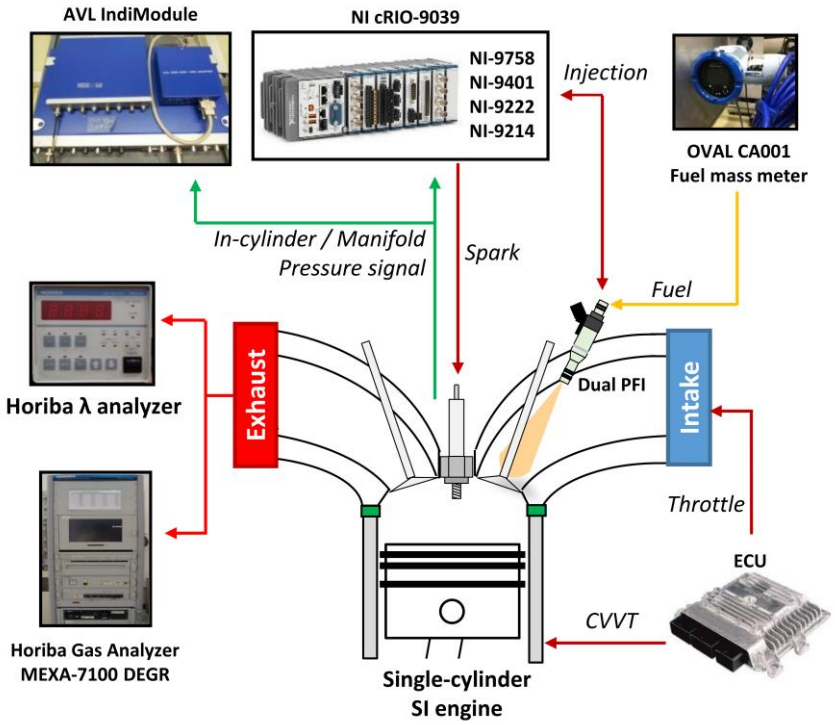

Fig. 1. Schematic diagram of the engine experiment.

Table 2. Test fuel properties [36]

Property		Value	Test method
H/C ratio		2.06	ASTM D 5291
Density [kg/m^3] at 15 °C		724.5	ASTM D 1298
Research octane number (RON)		91.5	ASTM D 2699
Lower heating value (LHV) [MJ/kg]		42.8	ASTM D 240-14
Oxygenate [mass %]		1.53	ASTM D 4815
Methanol content [mass %]		< 0.05	
Distillation Temperature [°C]	Initial boiling point	38	ASTM D 86-12
	10%	55	
	50%	83	
	90%	142	
	End point	197.6	

2.2 Experimental conditions

The engine was operated under various conditions to achieve wide applicability of the developed model. The engine speed was changed from 1,000 to 2,000 rpm, and the load was varied by altering the intake pressure and spark timing. The air-fuel ratio was maintained stoichiometric conditions by adjusting the fuel flow rate and intake pressure under while monitoring the lambda sensor output and exhaust emission. The knock incidence observed during the experiments ranged from 0% to 80%, depending on the operating conditions. One of the most important aims of this study was to ensure the validity of the model under different valve timing conditions; as valve overlap (VO) alters the residual gas fraction, which has a profound effect on the ignition delay of a reactant, the VO was varied from 0–40 CA by changing the intake valve timing. The ambient air, oil, and coolant temperatures were maintained at the same level during the experiment. The ranges of the operating parameters are summarized in Table 3. Fig. 2 displays the total 79 operating points used in this study in the three-axis domain for the engine speeds, loads, and spark timings.

Table 3. Test conditions

Engine speed	1000–2000 rpm
Spark timing	28 CA bTDC–4 CA aTDC
Engine load	4.58–9.5 bar
Intake pressure	0.6–1 bar
Air-fuel ratio	Stoichiometric ($\lambda = 1$)
Ambient temperature	25 ± 1 °C
Oil/Coolant temperature	85 ± 2 °C
Valve overlap	0–40 CA

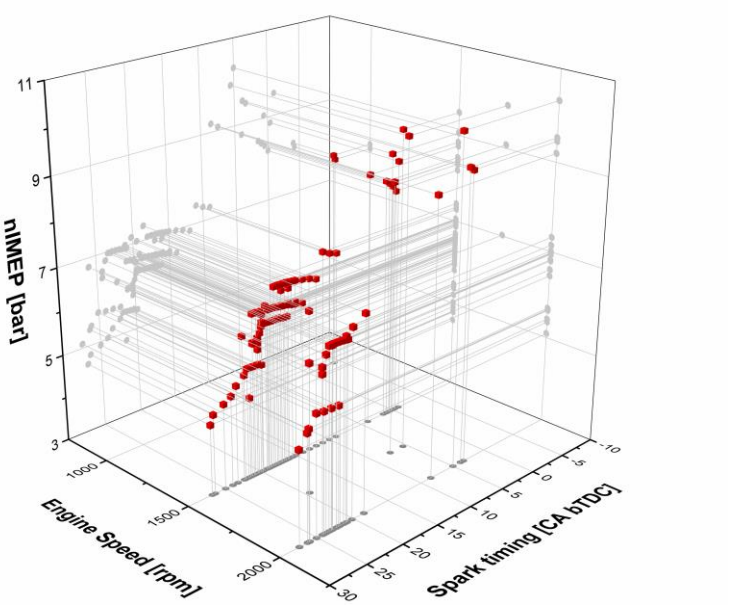

Fig. 2 Engine operating conditions.

2.3 Knock metric

The knock detection was performed during the experiment using an in-cylinder pressure transducer. A high-pass filtering method with a nine-point median filter was used to capture the pressure oscillation(s) generated by the

autoignition of the end-gas [22]. A 0.5 bar maximum amplitude of pressure oscillation (MAPO) threshold was used to determine the knocking cycle. Because the knocking behavior during engine operation is highly stochastic, every cycle shows a different knock intensity; therefore, a statistical approach is essential for determining the knock propensity, which is represented as a knock incidence. In this study, the knock incidence was calculated by dividing the knocking cycle number by a total cycle number of at least 2,000 [36, 37]. Eqs. 2 to 4 show the expressions for the knock metrics used in this study.

$$P_{med,n} = (P_{n-4} + P_{n-3} + \cdots + P_{n+3} + P_{n+4})/9, \qquad P_{filt} = P - P_{med} \tag{Eq. 2}$$

$$\left|P_{filt}\right| > 0.5\ bar \tag{Eq. 3}$$

$$Knock\ incidence = \frac{N_{knock}}{N_{total}} \times 100\ [\%] \tag{Eq. 4}$$

Determination of knock onset (KO) is critical for obtaining a refined ignition delay correlation. In this study, an artificial neural network (ANN) model was used to determine the KO from the in-cylinder pressure traces. The ANN KO model identified KO by scanning the in-cylinder pressure traces, as a human does. A detailed description can be found in a previous study [22]. The results from the KO model are shown in Fig. 3. The X-axis of the graph indicates the KO values as determined from per-cycle in-cylinder traces by a mouse-clicking method, i.e., by human labor. The Y-axis indicates the KO values as obtained from the ANN model. More than 10,000 random cases of cyclic data were used, and the model showed good performance for KO determination.

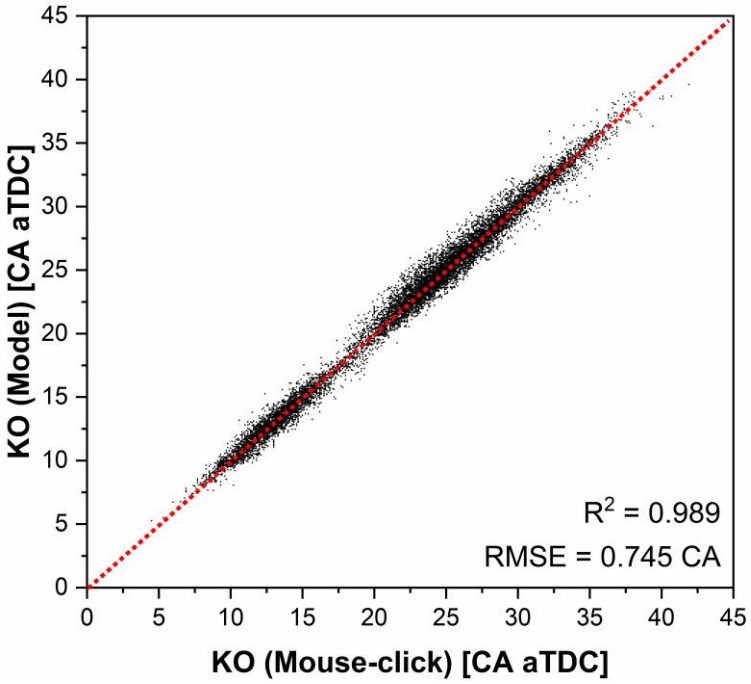

Fig. 3. Parity plot showing the relationship between artificial neural network (ANN)-based knock onset (KO) and human-based KO.

3. Modeling process for knock prediction

Fig. 4 shows a flowchart of the model developed in this study. As mentioned previously, the necessity of the in-cylinder pressure measurement was eliminated. This was achieved by an in-cylinder pressure estimation; the detailed procedure of this estimation is presented in the following sections. Then, the knock prediction model is described.

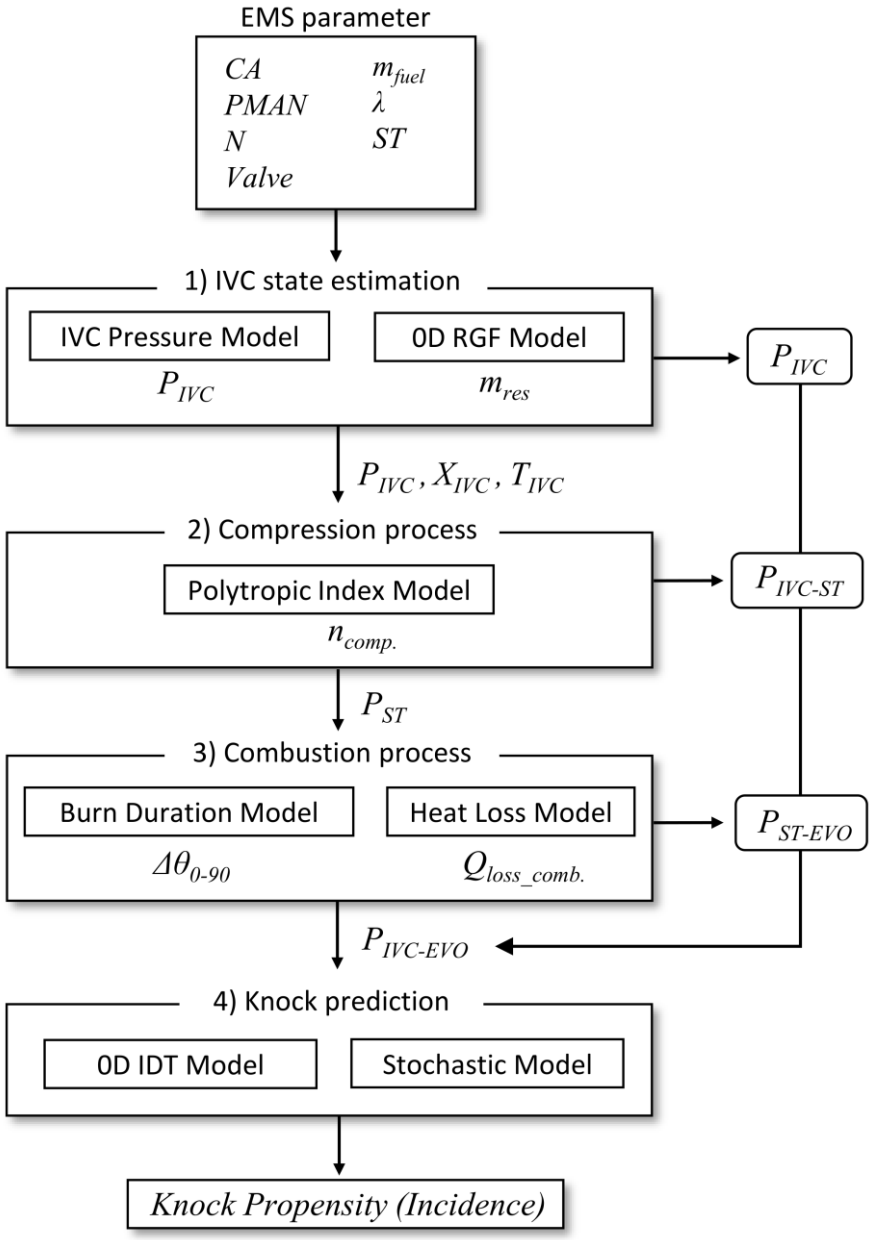

Fig. 4 Main steps of knock prediction process and modeling. Processes 1–3 generate predicted in-cylinder pressure from IVC to EVO, and knock prediction is carried out in process 4.

This section discusses four steps: 1) estimation of the thermodynamic conditions at the intake valve closing (IVC) timing, 2) modeling compression process, 3) combustion process, and 4) prediction of knock propensity.

3.1 Estimation of the intake valve closing (IVC) thermodynamic condition

An accurate estimation of the thermodynamic conditions at the IVC timing is essential for predicting the pressure during the closed cycle. High accuracy is required at this stage, as a small error can propagate and create a significant error after the compression and combustion processes.

Two main factors should be considered in the first stage: the pressure and reactant compositions. If the pressure and reactant compositions are adequately estimated, the temperature can be simply calculated using the ideal gas law, as shown in in Eq. 5.

$$T_{IVC} = \frac{P_{IVC}V_{IVC}}{(n_{fuel} + n_{air} + n_{res})\bar{R}} \quad \text{(Eq. 5)}$$

The pressure at the IVC (P_{IVC}) and mole number of the residual gas (n_{res}) are required, whereas the other parameters are available from the EMS. The following subsections describe the modeling approaches for obtaining P_{IVC} and n_{res}.

3.1.1 In-cylinder pressure at IVC

To obtain a good estimation of P_{IVC}, the process begins with the measuring the intake pressure using a manifold absolute pressure (MAP) sensor; the corresponding data is logged by the EMS. Table. 4 lists the previous models' and present work's linear correlations for the performance comparison. And the modeling results for the P_{IVC} estimation are displayed in Fig. 5. The figure contains 79 points of experimental data, which are averaged values of the 3,000 consecutive cycles for each operating condition. The x-axis indicates the actual pressure value as measured

with the MAP sensor, and the y-axis indicates the estimated P_{IVC} value from the linear correlations listed in the Table 4.

Table 4. Expressions for IVC pressure estimation

Model expression		Reference	Corresponding figure
$P_{IVC} = P_{int@IVC}$	(Eq. 6)	-	Fig. 4(a)
$P_{IVC} = P_{int@IVC} + C_1 + C_2 Speed$	(Eq. 7)	Eriksson et al. [38]	Fig. 4(b)
$P_{IVC} = P_{int@IVC} + C_1 + C_2 Speed + C_3 OF$	(Eq. 8)	Present work	Fig. 4(c)

Fig. 5(a) shows the deviation between the measured P_{IVC} (x-axis) and estimated (modeled) P_{IVC} (y-axis) when it is assumed that the P_{IVC} equals the intake manifold pressure (P_{int}) at the IVC. This assumption holds only when the IVC timing coincides with the bottom dead center (BDC), as the in-cylinder pressure is pegged using the P_{int}. In reality, the IVC timing occurs after BDC, and the compression of the in-cylinder gases begins from the BDC. Thus, additional factors must be considered to correctly predict the P_{IVC}. As the VO decreases to a negative value, the intake pressure becomes lower than the in-cylinder pressure. Owing to the density change, the volumetric efficiency is larger in low-VO cases; therefore, the simple equivalence model underestimates the pressure. Additionally, the change in the engine speed is not considered.

One important factor is the engine speed. This is because at higher engine speeds, the compression of the in-cylinder gases increases after BDC. To this end, Eriksson et al. [38] factored the engine speed into the correlation, as shown in Eq. 7. Fig. 5(b) illustrates the results from Eriksson's model by empirically calibrating the coefficients (C_1 and C_2) with the experimental result. An improvement in the P_{IVC} prediction can be observed compared to the results shown in Fig. 5(a). However, a discrepancy is still observed for highly throttled conditions. This is

attributable to the insufficient consideration of the change in the VO, which has a pronounced impact on the residual gas fraction (RGF) at lower intake manifold pressure conditions.

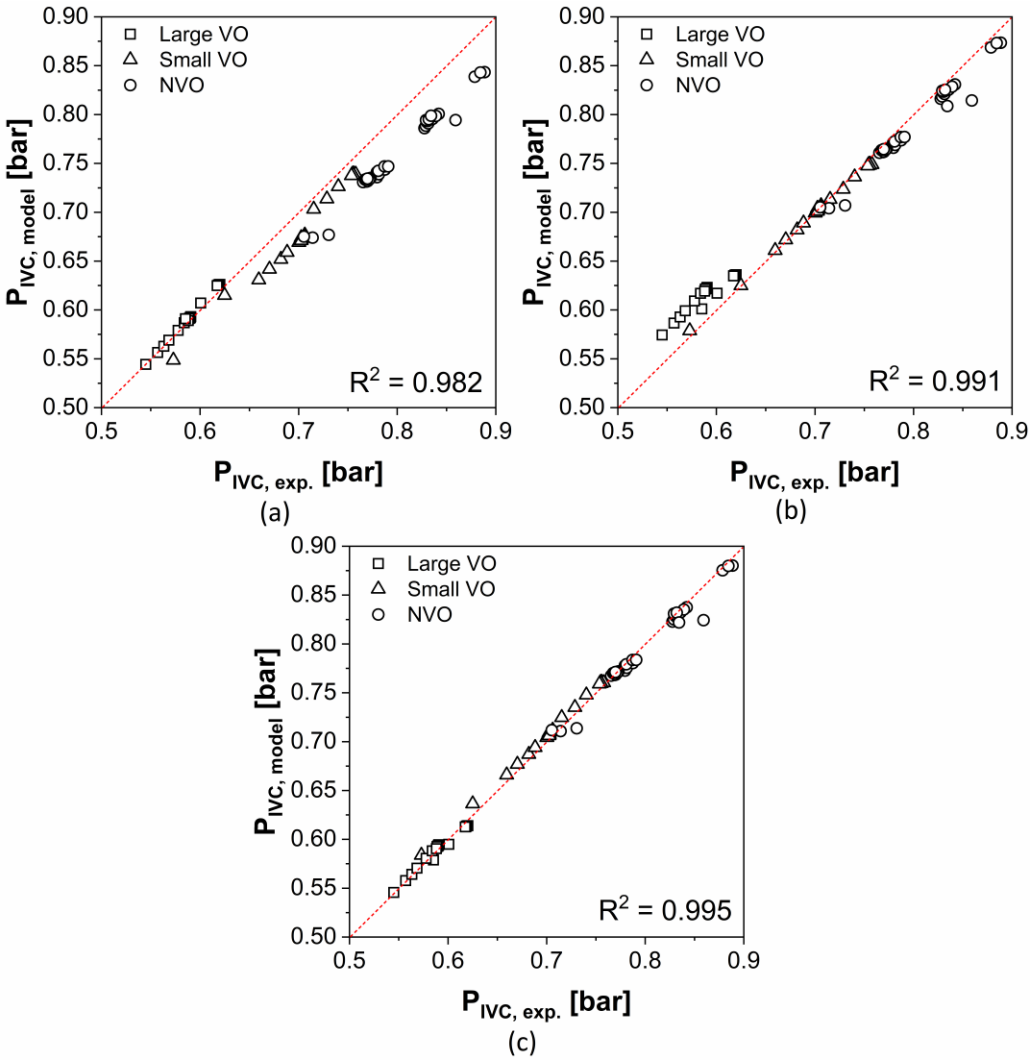

Fig. 5. Pressure estimation at intake valve closing (IVC); refer to Table 4 for details.

Therefore, in this study, to further improve the accuracy of P_{IVC} prediction, a new correlation was proposed. This correlation incorporated the change effect in the VO by introducing the overlap factor (OF). The OF was first suggested by Fox et al. [39] for the 0D RGF model. To simplify the model for potential implementation in the EMS, OF was utilized rather than the derivative RGF value. With the addition of the OF, as shown in Eq. 8, a better prediction of P_{IVC} could be achieved after the coefficient tuning with the experimental data, as shown in Fig. 5(c).

3.1.2 Residual gas fraction

Several 0D models have been developed for estimating the RGF. As shown in Eq. 9, Fox et al. [39] introduced a model for considering the residual gas in the cylinder before the intake valve opens and the residual gas arising from backflow into the intake port during VO.

$$RGF = RGF_{trapped} + RGF_{backflow} \quad \text{(Eq. 9)}$$

All the 0D RGF models, including the one suggested in this study, employ the concept above. Kale et al. [40] revised Fox's model by considering additional factors to include the physics of the gas exchange processes, e.g., the intake valve opening and exhaust valve closing timings relative to top dead center (TDC) of the VO period, and the timing at which the valve-curtain areas of the intake and exhaust valves became the same.

Fig. 6 shows the validation results from the 0D RGF models: (a) Fox, (b) Kale, (c) the present work. In the figure, the RGF values obtained from 0D model are plotted against those obtained from a one-dimensional (1D) simulation. The 1D engine simulation was performed using GT-Power v2018. The following steps were introduced into the 1D simulation. First, motored operation instances with various valve timings and engine speeds were validated to best characterize the intake and exhaust wave dynamics of the engine used in this study. Second, the pressure traces from 14 cases of experiments with combustion were reproduced by tuning the multipliers in existing combustion model (SITurb) and heat transfer model (Woschni [41]) using a genetic algorithm, and minimizing the sum of squared error

between the modeled pressure and experimental pressure during the combustion period. Lastly, using a design of experiments approach, a dataset of 1200 points was generated by varying the engine parameters (speed, spark timing, input charge amount, and valve timings) with the optimized GT-Power engine model. The same process is shown and well explained in previous study [22] so detailed optimization process was excluded in this paper for brevity. Among them, 136 cases were excluded owing to an overly advanced combustion phasing (CA50 < 5 CA after TDC) highly unlikely to be used in a production engine. Accordingly, a dataset of 1064 total elements was used. The coefficients in the proposed 0D RGF model were calibrated using the function *fmincon* in MATLAB.

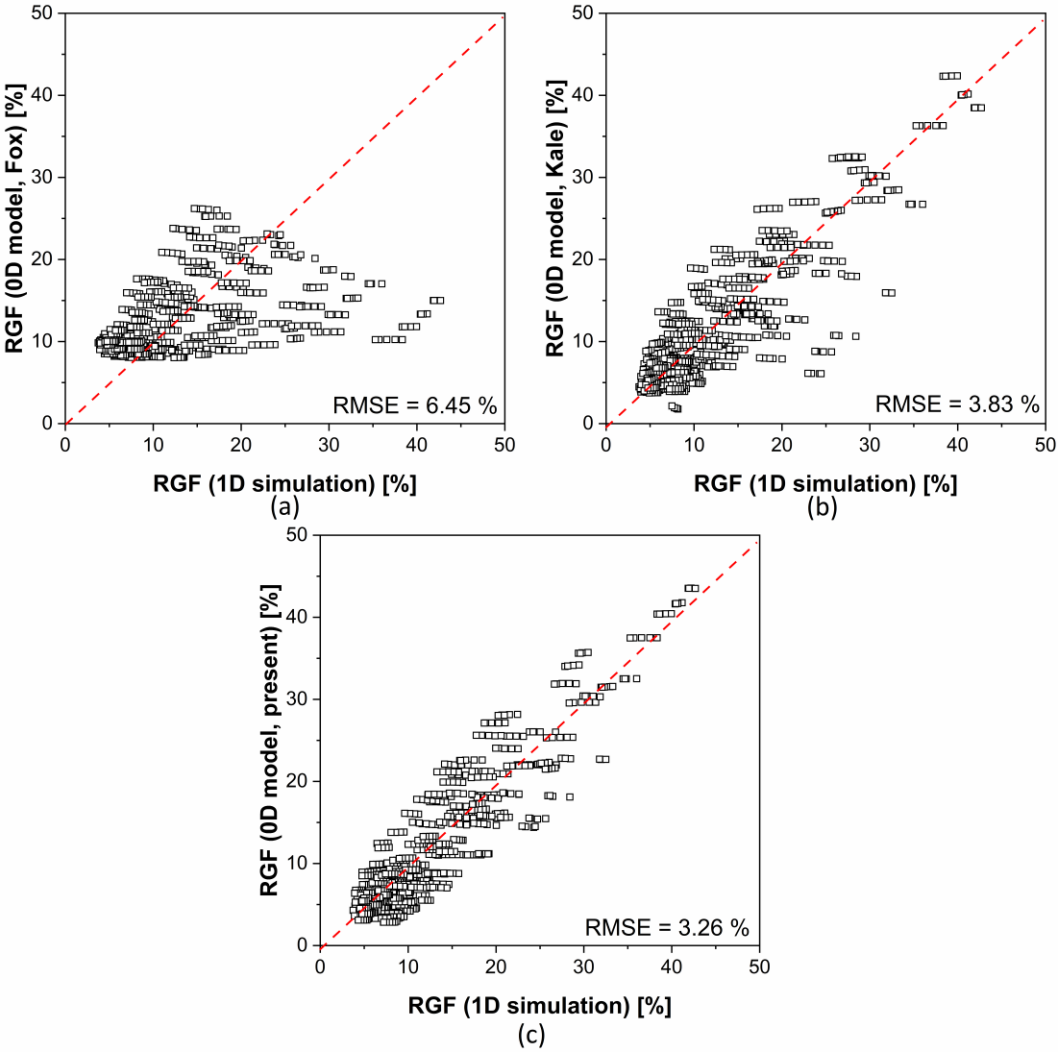

Fig. 6. 0D RGF models; (a) Fox et al. [39]; (b) Kale et al. [40]; (c) Present work.

As seen in Figs. 6(a) and 6(b), Kale's model shows a remarkable improvement compared to the original model proposed by Fox et al. In Kale's model, two OFs are calculated for each of the trapped RGF and backflow RGF: the non-speed-dependent OF (OF_{ns}) and speed-dependent OF (OF_s). However, large discrepancies remain, particularly for cases with high volumetric efficiency. A high volumetric efficiency value resulted in a negative OF

during the calculation, contributing to the underestimation of the RGF. In this study, the impact of the volumetric efficiency on the OF was expressed using an exponential function to prevent underestimation, and the modified equations for OF are suggested as the Eqs. 10 and 11. Fig. 6(c) shows the improved model as suggested in this study, with a slightly better agreement.

$$OF_{trapped,ns} = C_2(OF_{IN} - OF_{EX}) + {\eta_v}^{C_3}\phi$$
$$OF_{trapped,s} = C_4 OF_{IN} + C_5 OF_{EX} + {\eta_v}^{C_6}\phi + C_7 \quad \text{(Eq. 10)}$$

$$OF_{backflow,ns} = C_9(OF_{TDC,IN} - OF_{TDC,EX}) + C_{10}(OF_{IN} - OF_{EX})$$
$$OF_{backflow,s} = C_{11}(OF_{IN} + OF_{EX}) + C_{12}(OF_{TDC,IN} + OF_{TDC,EX}) + {\eta_v}^{C_{13}}\phi \quad \text{(Eq. 11)}$$

3.2 Compression process

The primary objective of this submodel was to predict the in-cylinder pressure at the spark timing (P_{ST}). The evolution of the in-cylinder pressure during the compression stroke can be predicted using the thermodynamic state at the IVC (obtained as discussed in the previous section) and a polytropic assumption. A pertinent determination of the polytropic index with the assumption of a polytropic process can lead to successful modeling. However, if the polytropic index is simply assumed to be the same as the specific heat ratio calculated at the end of the previous section, a difference can arise (with a maximum of approximately 15%) in the pressure value at the end of the compression process. In addition, error sources remain, such as the heat loss owing to heat transfer.

Therefore, an adjustment for the polytropic index is necessary to reflect the actual conditions; in this study, a novel methodology suggested for a diesel engine by Lee et al. [31] was adopted, with a minor modification. The polytropic index during compression (n_{comp}) is expressed as a function of the isentropic exponent (n_{isen}), heat loss ($Q_{loss\_comp.}$), and slope (S), as shown in Eq. 12. The isentropic exponent (n_{isen}) is the average polytropic index, assuming an adiabatic process. The suggested correlation of the isentropic exponent is shown in Eq. 13, where CR_{eff} is the effective compression ratio until the spark timing (V_{IVC}/V_{IGN}). The isentropic exponent was calculated

with the thermodynamic state, and the polytropic index during the compression was extracted from the pressure-volume profile during the compression process. The heat loss during compression is dominated by convective heat transfer; therefore, Eq. 14 was adopted, whereas the initial wall temperature T_w was set at 393 K for all operating conditions. The slope (S) is the rate of change of the polytropic index ($n_{comp.}$) with respect to $Q_{loss\_comp.}/T_{IVC}$, and the correlation is suggested by Eq. 15. Coefficients in Eq. 14 were tuned by matching the heat loss data achieved from the experimental result, and the coefficients in Eq. 15 were eventually adjusted in Eq. 12 thereafter. The representative pressure (P) and in-cylinder average temperature (T) in Eq. 15 are the values at the end of compression with the isentropic assumption using n_{isen}, considering that heat transfer during compression occurs mostly at the end of the stroke. Instead of the bore and swirl ratio terms used to characterize diesel engines in the previous study, a modified relationship ($u = stroke \cdot rpm/60$) was used to incorporate the effect of the tumble motion in modern gasoline engines. *fmincon* function in MATLAB was also used in this stage. The pressure was predicted using the polytropic assumption shown in Eq. 16, with the adjusted polytropic index as derived from Eqs. 12 to 15.

$$n_{comp.} = n_{isen.} + \frac{Q_{loss\_comp.}}{T_{IVC}} S \quad \text{(Eq. 12)}$$

$$n_{isen.} = C_1 {T_{IVC}}^{C_2} {\gamma_{IVC}}^{C_3} {CR_{eff}}^{C_4} \quad \text{(Eq. 13)}$$

$$Q_{loss\_comp.} = \frac{C_5 P^{0.8} u^{0.8} T^{-0.55} (T - T_w)}{N \cdot m} - C_6 \quad \text{(Eq. 14)}$$

$$S = C_7 {CR_{eff}}^{C_8} (T_{IVC})^{C_9} \quad \text{(Eq. 15)}$$

$$P_{model} = P_{IVC} \left(\frac{V}{V_{IVC}} \right)^{n_{comp.}} \quad \text{(Eq. 16)}$$

Fig. 7 shows a comparison between the measured and predicted P_{ST}. Across all experimental data acquired in this study, an excellent agreement is achieved; the R^2 value is 0.9986, and the root mean square error (RMSE) is 0.078 bar.

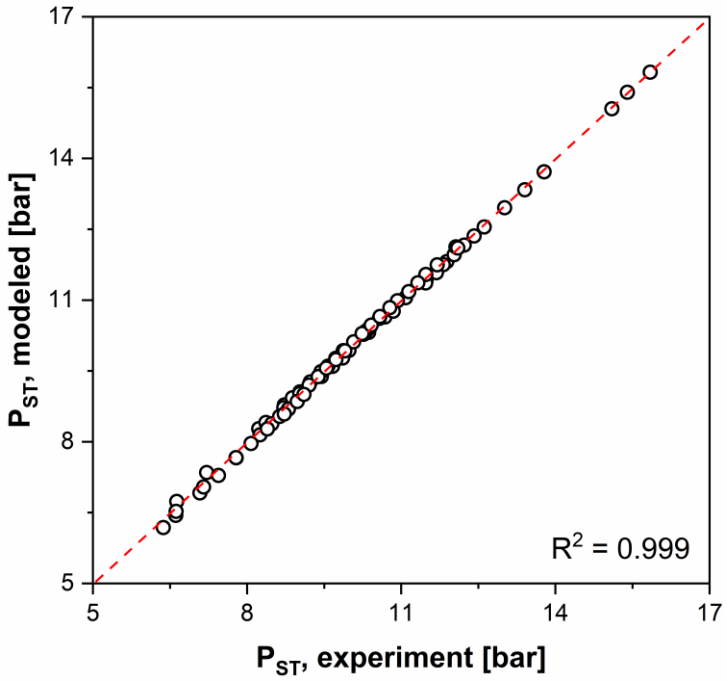

Fig. 7. Correlation of in-cylinder pressure values at spark timing: model vs. experimental result.

3.3 Combustion process

This section focuses on modeling the evolution of the in-cylinder pressure during the combustion process, starting from the value of P_{ST} obtained from the submodel described in the preceding section. The approach taken in this study uses a representative heat release curve and adjusts it accordingly for each operating condition, based on the estimated burn duration and heat loss for a given condition.

3.3.1 Representative heat release curve

Depending on the engine operating conditions, the in-cylinder phenomena vary, so the rate of the combustion process changes. The variations are caused by changes in operating parameters such as the spark timing, fuel injection, and trapped air mass. In this study, to model a combustion process encompassing such variations, an approach using a representative curve was adopted. First, the average burn rate during combustion was assumed to be represented by a Wiebe function, as shown in Eq. 17. Subsequently, several parameters in Eq. 17 were normalized to obtain a generic expression, as shown in Eq. 18. The total amount of heat released was normalized by the input fuel energy value after subtracting the net heat loss, and the combustion angle parameter ($\theta - \theta_{ST}$) was normalized by the burn duration ($\Delta\theta_{0-90}$).

$$\frac{Q_{net}(\theta)}{Q_{fuel} - Q_{loss}} = 1 - exp\left[-a\left(\frac{\theta - \theta_{ST}}{\Delta\theta_{0-90}}\right)^{m+1}\right] \quad \text{(Eq. 17)}$$

$$Q_{norm}(\theta) = 1 - exp[-\mathrm{a} \cdot (\theta_{norm})^{m+1}] \quad \text{(Eq. 18)}$$

The burn duration was defined as the time spanned from CA0 (spark timing) to CA90 (combustion phasing at which 90% of the reactant was consumed). This was because the Wiebe expression asymptotically approaches unity, owing to the nature of a sigmoid function. Any indicator posterior to the mass fraction burned (MFB)85 was found as feasible in this study; however, no timing prior to MFB85 could be used, owing to the knock criterion suggested later in this study.

Fig. 8(a) shows the MFB curves from the individual operating conditions. Each curve was obtained by averaging over 2,000 cycles. In Fig. 8(b), the MFB curves presented in Fig. 8(a) are repeated after normalization (as explained above). The dashed line in Fig. 8(b) is the representative MFB curve used in this study, and was obtained by simply averaging all of the normalized curves. Note that the y-axis only spans to 0.9 as explained above. Although not all the data perfectly collapses onto the representative curve, the deviation from the representative MFB curve is not significantly large, within the 0.1 MFB and 0.05 CA ranges. This provides a basis for utilizing the representative

MFB curve to represent the average burn rate. Furthermore, this simplification is advantageous to speeding up the calculations. This approach will hold its accuracy as long as the engine is operated within a reasonable operating parameter domain. However, the current method is not fully validated at a boosted condition, e.g., where significantly retarded spark timing is used. However, the boosted condition is out of the scope of the current study.

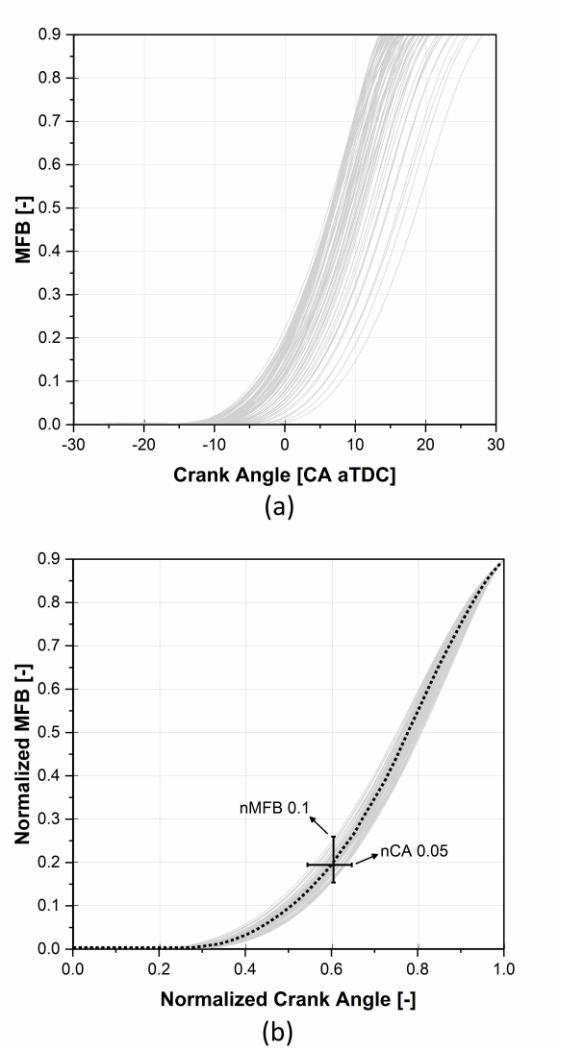

Fig. 8. (a) Individual MFB curves plotted against CA. (b) Normalized MFB curves and a representative curve of normalized MFB curves.

3.3.2 Modeling of heat loss during combustion (Q_{loss_comb})

This section describes how the heat loss ($Q_{loss\_comb.}$) and burn durations ($\Delta\theta_{0-90}$) were modeled. These parameters are needed to convert Eq. 18 back to Eq. 17 to compute the in-cylinder pressure during combustion.

A precise measurement of the wall heat loss is not trivial in an engine, and estimating the wall heat loss using high-fidelity 3D computational fluid dynamics across hundreds of conditions is costly. However, because the main goal of this study was to better estimate the in-cylinder pressure, $Q_{loss\_comb.}$ was estimated in a simplistic manner to achieve reasonable accuracy.

$$Q_{loss\_comb.} = C_1 {m_{fuel}}^{C_2} Speed^{C_3} {\theta_{ST}}^{C_4} \quad \text{(Eq. 19)}$$

Eq. 19 was introduced to model the heat loss in this study. The majority of the heat loss was owing to convective heat transfer, and was determined based on the temperature gradient between the gas and wall, as well as the convection coefficient. Thus, in the proposed model, the convection coefficient was represented by the engine speed, and the fuel mass and spark timing were used to represent the in-cylinder pressure and temperature. For the $Q_{loss\_comb.}$ calculation, the timing of the end of combustion was assumed to be 10 CA after the time at which the in-cylinder pressure multiplied by the cylinder volume reached the maximum value, following the methodology proposed in [42]. Thereafter, the Woschni [41] heat transfer model was tuned to integrate the apparent total heat release to match the total combusted fuel energy. The combustion efficiency was assumed as a constant value (0.98), as it could not be obtained from the EMS. The coefficients were calibrated using the *fmincon* function in MATLAB.

Fig. 9 shows the correlation between the experimental heat loss result (aforementioned calculated Woschni loss) and modeled heat loss result. The result shows a reasonably accurate correlation, with an R^2 value of 0.958. However, the accuracy of the proposed model is reduced in the lower load region; this is attributed to the change in the RGF, which significantly affects the heat loss during the cycles.

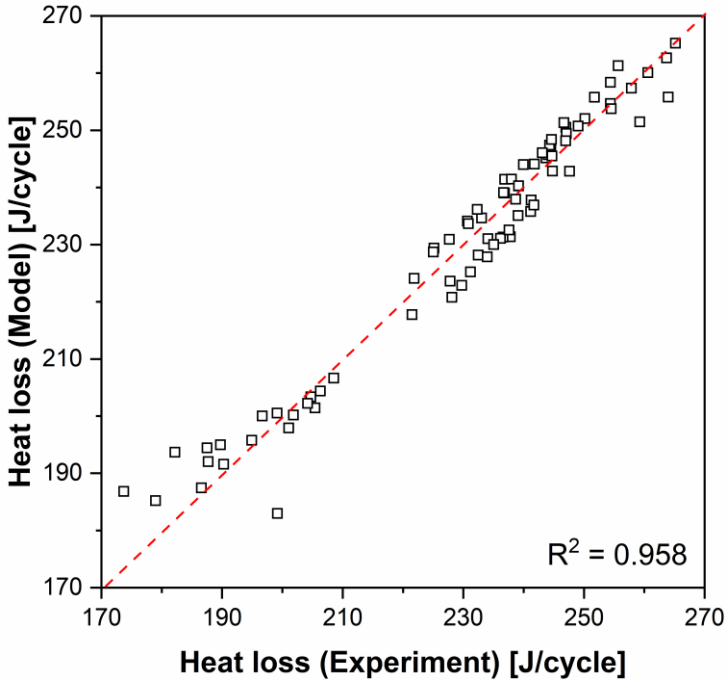

Fig. 9 Parity plot of heat loss model results.

3.3.3 Modeling burn duration ($\Delta\theta_{0-90}$)

In addition to the estimation of the heat loss (Q_{loss}), modeling for the burn duration was also necessary to construct the heat release in Eq. 17 from the normalized Eq. 18. A model suggested by Bonatesta et al. [43] was employed in this study; its expression is shown in Eq. 20, where ρ is the density at spark timing, S_{piston} is the mean piston speed, x_r is the residual gas fraction, and θ_{ST} is the spark timing in the CA before TDC.

$$\Delta\theta_{0-90} = C_1\rho^{C_2}\left(1-\frac{C_2}{\sqrt{S_{piston}}}\right)\left(\frac{C_3}{1-2.06{x_r}^{0.77}}\right)^{0.85}\left(C_4{\theta_{ST}}^2+C_5\theta_{ST}+1\right) \quad \text{(Eq. 20)}$$

Fig. 10 shows the correlation between the calculated burn duration and modeled burn duration. The coefficients were newly calibrated for this study using the *fmincon* function in MATLAB and experimental data. As a result, an R^2 value of 0.856 is achieved. It does not seem that only having one term with piston can represent the whole

conditions' turbulent flame speed. In this respect, an employment of simplified chemical mechanism [34] would be beneficial, however a further study would be needed for better accuracy and applicability to a wider operating range. However, as mentioned earlier, many sub-models are established for holistic processes in this study, and therefore pursuing the utmost accuracy of each model was avoided to more focus on this study's main objective, i.e., revealing the feasibility of knock propensity prediction.

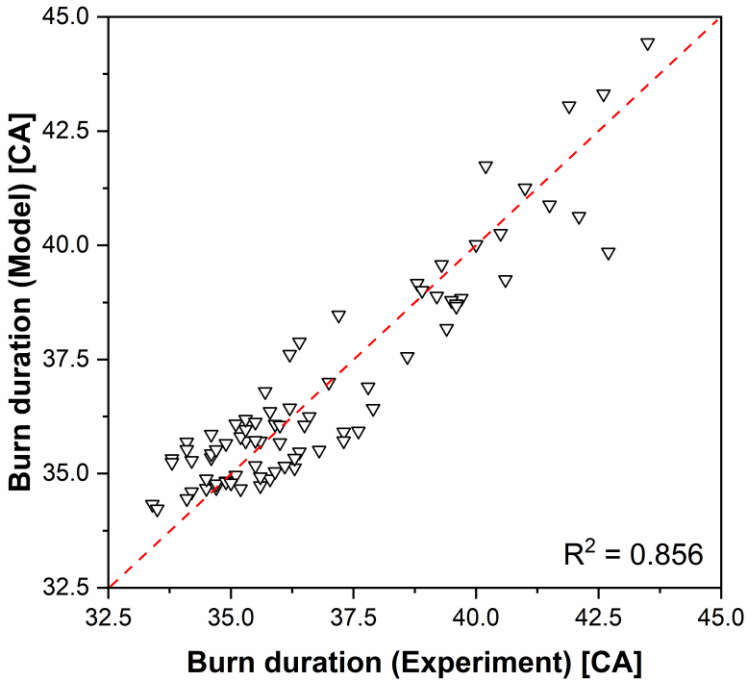

Fig. 10 Parity plot of burn duration model results.

3.3.4 Construction of estimated in-cylinder pressure

The previous sections describe how to estimate Q_{net} for a given operating condition using the burn duration model and heat loss model. This section describes how the in-cylinder pressure is reconstructed during combustion,

using the burn rate profile obtained from Eq. 17. The implicit method shown in Eq. 21 was applied in this study; this is the exact opposite of the method in the combustion analysis, as can be seen from the equation.

$$P_n = \frac{\frac{dQ_{net}}{d\theta} - \frac{\gamma}{\gamma - 1} P_{n-1} \frac{dV}{d\theta}}{\frac{1}{\gamma - 1} V_{n-1} \frac{1}{\Delta\theta}} + P_{n-1} \quad \text{(Eq. 21)}$$

The specific heat ratio (γ) changes primarily based on the in-cylinder composition and temperature. However, the simplified calculation was prioritized to secure the applicability of this model to the EMS system for real-time control of knock and autoignition. Therefore, a constant value of 1.3 was tried for the specific heat ratio during combustion analysis and in-cylinder pressure modeling.

Fig. 11 illustrates predicted in-cylinder pressure finalized by the modeling, as overlaid on the experimentally measured pressure traces. Eight examples are randomly selected. The proposed modeling yields results that show a distinctive agreement in various operating ranges of the engine speed, valve timing, and spark timing. It shows less accuracy with retarded combustion phasing (top-right figure case) relative to other conditions; this issue becomes larger when the spark timing is retarded more significantly, e.g., a wide-open throttle (WOT) condition. The estimation of the in-cylinder pressure in this study was simply based on the Wiebe-functioned heat release profile to render the potentiality of the conceptual idea; the aforementioned limitation of the modeling is attributed to a pre-heat release phenomenon near TDC, owing to the relatively high compression ratio. In observance with the different behaviors in the WOT condition, an incremental study is required to further improve the accuracy, i.e., by incorporating low-temperature reactions at a higher compression ratio.

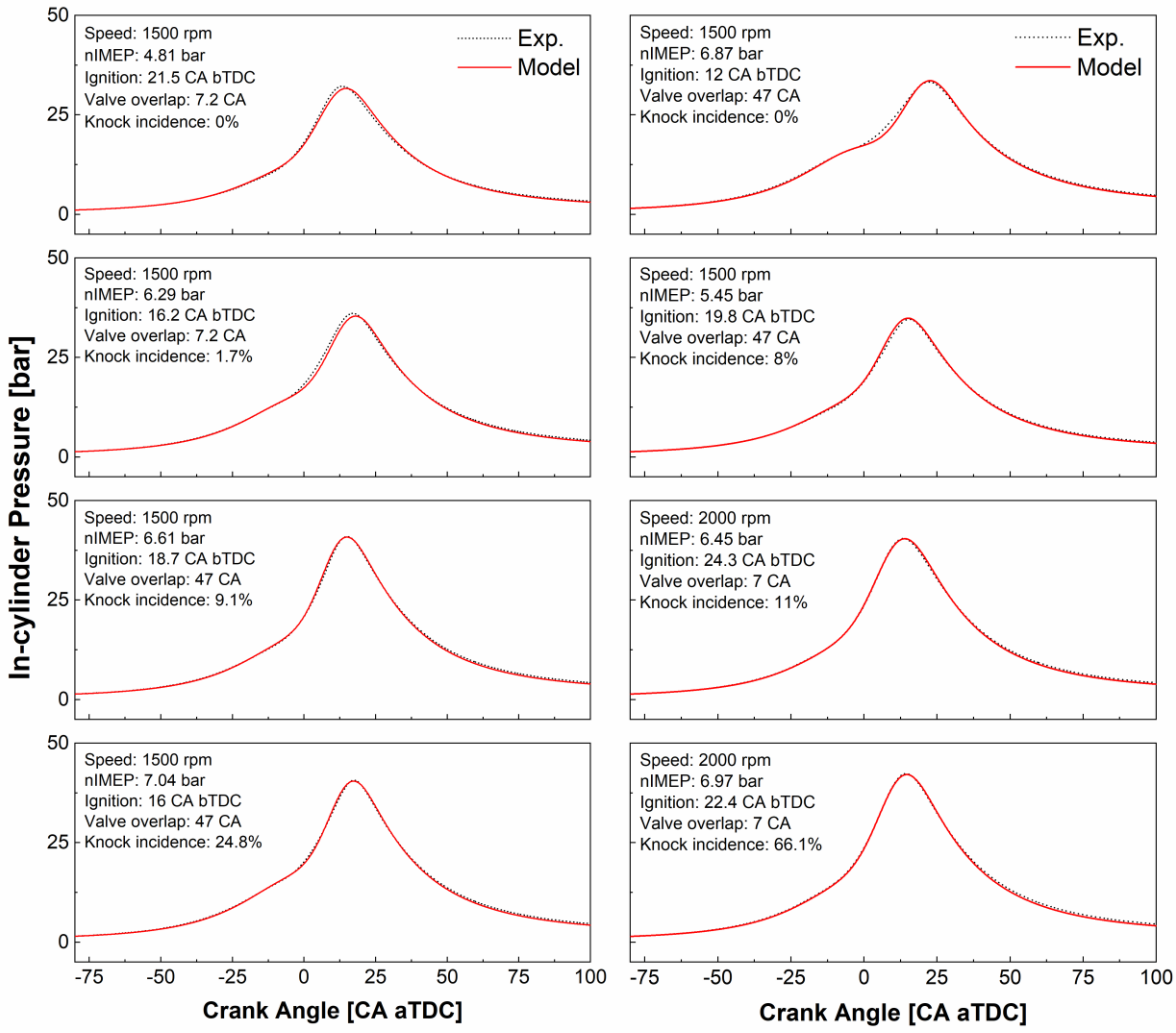

Fig. 11 Comparison of in-cylinder pressure predicted by developed model (solid red) and measured experimentally and averaged over 2,000 cycles (dashed black) under various operating conditions. The information on engine operating conditions is annotated in the individual graphs. Only eight operating points are presented.

3.4 Knock model

The knock prediction in this study is established using the estimated in-cylinder pressure. The estimated in-cylinder pressure is utilized to compute the reactant temperature, which is required to calculate the ignition delay using a 0D correlation.

3.4.1 0D ignition delay correlation

$$\tau = C_1 \left(\frac{P}{T}\right)^{-C_2} (1 - \chi_{EGR})^{-C_3} \lambda^{-C_4} exp\left(\frac{C_5}{T}\right) \quad \text{(Eq. 22)}$$

The 0D ignition delay model used in this study is expressed by Eq. 22. This correlation was proposed by Chen et al. [20] to incorporate the effects of variations in the air-fuel ratio and external exhaust gas recirculation (EGR) rate. However, in the present work, the engine experiment was performed under stoichiometric conditions, i.e., without external EGR. Thus, the equation was simplified by tuning only three coefficients in this study. The coefficients were calibrated using genetic algorithm-based optimization [20, 22], by minimizing the RMSE between the experimental KO data (derived from the ANN model in Section 2.3) and the calculated KO using the suggested correlation. Combining the equation with the Livengood-Wu integral method [13] provides the autoignition timing, i.e., the KO timing at which the right-hand side of Eq. 1 reaches unity; the ignition delay τ is in millisecond units, and this timing is predicted based on the KO.A genetic algorithm that minimizes the RMSE between model-predicted KO and experimental KO was used to calibrate the coefficient. The population was one thousand, and the generation limit was set to 25. Crossover and mutation multipliers were set 0.7 and 0.3, respectively. Fig. 12 shows the validity of the calibrated 0D ignition delay correlation. The horizontal axis is the KO from the experiment, and the vertical axis indicates the KO from the knock model combining Eqs 1 and 22. An RMSE of 1.03 CA is shown; as the calculation was conducted based on per-cycle analysis, a satisfactory correlation is achieved. However, the result of the Livengood-Wu integral does not necessarily indicate that the autoigniting cycle results in a knocking

cycle. Therefore, a new method based on a knock criterion is proposed. The effect of fuel property on autoignition was out of scope. However, Eq. 22 can be modified as many previous studies on 0D ignition delay correlations incorporated using octane number terms [16, 20]. A further study is required on this perspective, but it is expected to secure reasonable accuracy after recalibration of the model considering the previous studies' validation results.

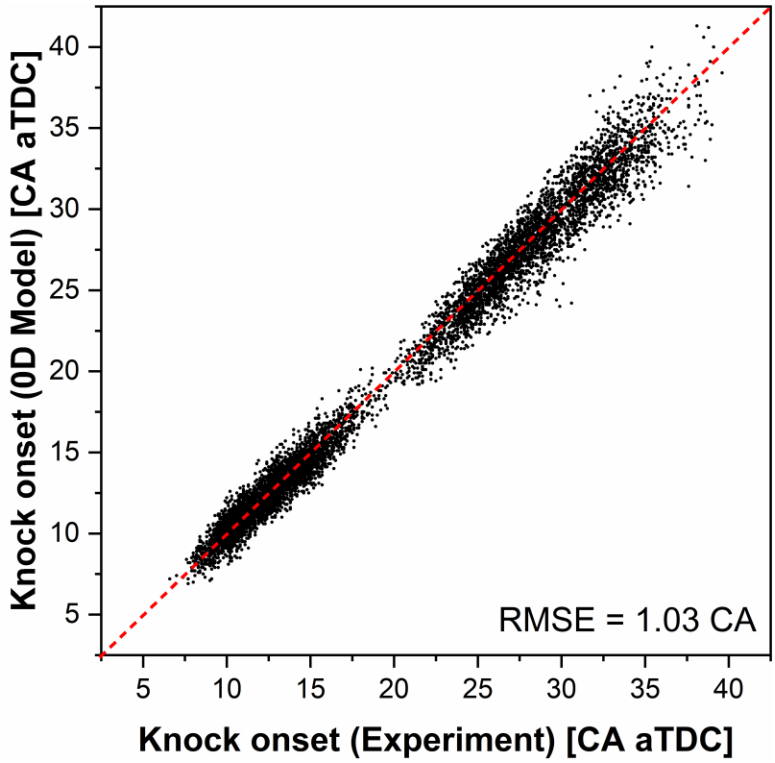

Fig. 12 Validity of 0D ignition delay model.

3.4.2 Knock criterion

Fig. 13 shows the relation between the experimental knock incidence and average MFB at KO. The KO was determined using the ANN, as explained in the previous section. The knocking cycle numbers are small for weakly knocking cases (low-knock-incidence cases); thus, the correlation between the average MFB at KO and knock

incidence is weaker for the cases with lower knock incidence, as shown in the figure. Nevertheless, a strong correlation (indicating a higher knock incidence) is shown in cases where the residual fuel-air mixture amount is larger at KO. Furthermore, it can be seen that the end-gas autoignition does not necessarily develop into an acoustic knock if the autoigniting end-gas mass is less than 15% of the total in-cylinder charge mass.

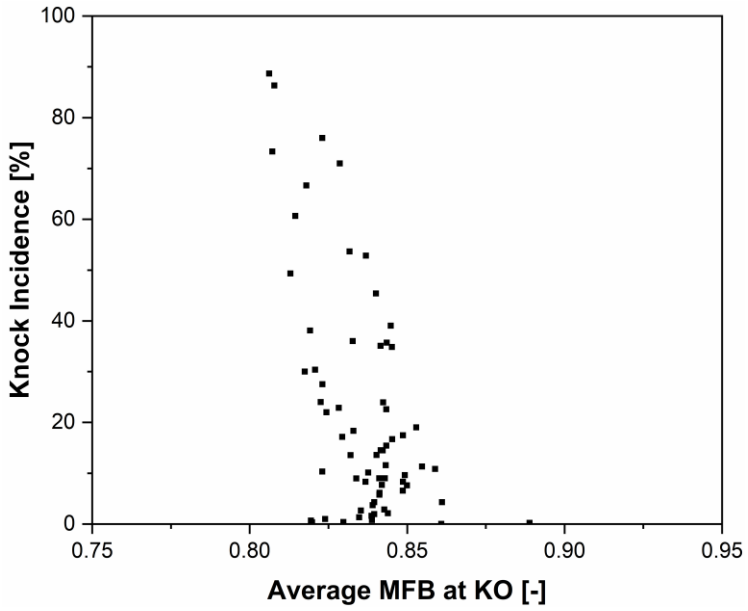

Fig. 13 Knock incidence and MFB.

It was determined that a given cycle was knocking when MAPO exceeded 0.5 bar. The use of different criteria for knock detection may lead to a different correlation from shown in Fig. 13. However, the conclusion (that a certain amount of end-gas mass needs to be autoigniting to incur acoustic knock) does not change. Another variable for the correlation shown in Fig. 13 is the fuel effects, as presented in [44-46] where the amounts of end-gas mass autoigniting to incur knock are different for compositionally dissimilar fuels. However, consideration of the fuel effects is beyond the scope of the current study.

Fig. 14 illustrates the relationships between the predicted KO and various burn points. The experimental data can be separated into two different groups: a group with higher incidence (> 15%, apparent knock which needs to be avoided), and a group with low knock incidence (< 5%, i.e., weak knock, and less likely to be perceived by driver). The results shown in this figure can be utilized to determine which burn point can better distinguish between the two regimes of knock incidence. This procedure is needed because engines can tolerate low knock incidence; moreover, this approach does not require active control of the spark timing retardation, which would result in an unnecessary loss of efficiency.

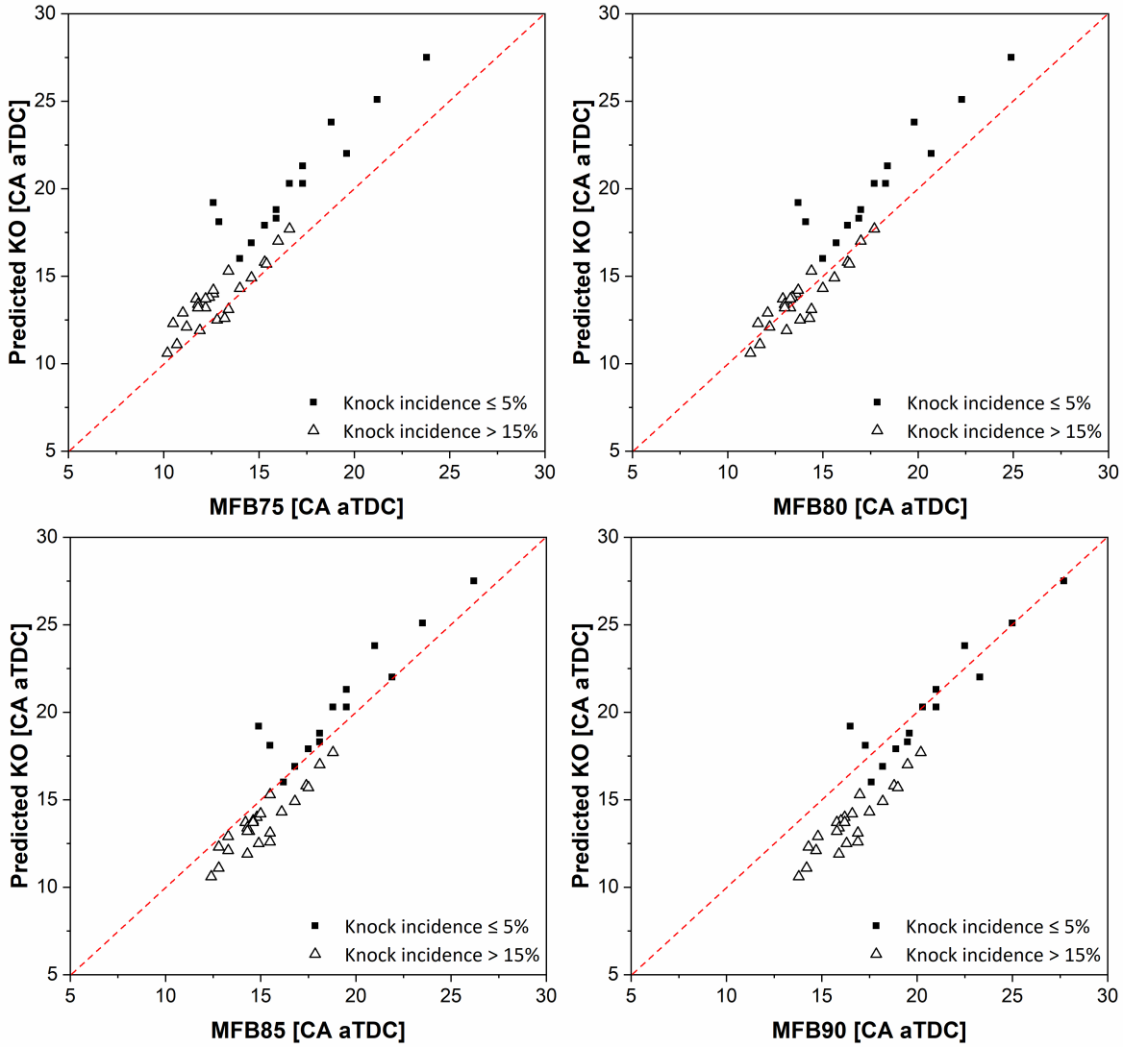

Fig. 14 Comparison between autoignition timing predicted using Livengood-Wu integral and various burn points; burn points were varied from MFB75 to MFB90 in an increment of 5 unit-%.

When a data point is located above the identity line (red dotted), it indicates that the predicted autoignition timing (model-based KO) is preceded by the burn point used in the plot. The opposite is true when the predicted autoignition timing is below the identity line. It was found that MFB85 is the best burn point for distinguishing

between knock (> 15%) and non-knock (< 5%) cases. Thus, the burn point of MFB85 is determined to be the value for disambiguating the apparent knocking condition from the less-likely-perceived knocking condition for the combination of engine and fuel used in this study. This information can be utilized to consider the stochastic nature of knock occurrence, as explained in the following section. It was not validated that this proposed criterion is general throughout the engines on the market, and the determined criterion can be changed when the methodology for modeling varies. In a future study, a sensitivity analysis is necessary to evaluate the tolerances of the variables and/or chosen methodologies lying in all of the modeling processes including the stochastic modeling presented in the next.

4. Stochastic modeling

0D modeling does not possess full flexibility for replicating the cyclic variation; knock is a stochastic phenomenon, and requires a parameter such as knock incidence to describe the probability of knocking cycles within a number of operating cycles. To replicate the stochastic nature of the knocking phenomenon, a stochastic modeling approach was employed, using the Wiebe function. The two Wiebe parameters, a and m in Eq. 17, were chosen as the perturbation factors for the stochastic model. The information on the combustion duration ($\Delta\theta_{0-90}$) and spark timing(θ_{ST}) was utilized to estimate the burn rate, as the stochastic model was intended to predict the probability of knock occurrence during combustion.

Fig. 15(a) shows a 2D probability density map of the Wiebe parameters a and m, where all individual single-cycle data are presented. Note that the contour plot is not continuous to display the discretization of the parameters. In general SI engines, the Wiebe parameter a generally has a value of approximately four and is followed by the relationship of $a = -ln(1 - X_{comb})$, where X_{comb} is the combustion efficiency [42]. The probability density of a has a mean value of 2.418 in its lognormal distribution; this is attributed to the 0.9 end value of the Wiebe curve of the representative heat release rate curve, as described earlier in Section 3.3.1. Based on the nature of the Wiebe

function, the MFB value at the time when the fastest combustion speed in a cycle is expressed as $X_b = 1 - exp(-m/(m+1))$; the engine used in this study showed $X_b = 0.55$, approximately.

Fig. 15(b) presents a binary map of knock occurrence derived from the aforementioned knock criterion (MFB85) and stochastic modeling. Only one example is shown for clarity. Discretization of the stochastic modeling parameters (*a* and *m)* were set to 0.25 and 0.1, respectively. *a* ranged from 0.5 to 5.5, and *m* ranged from 3.0 to 5.0. Predicted KO was calculated using the predicted in-cylinder pressure and knock model, depending on the values of *a* and *m* of the Wiebe function. MFB85 was calculated based on the predicted in-cylinder pressure. A comparison of the predicted KO and MFB85 provides a binary map, as shown in the figure; the knock region is indicated by black, and the non-knock region is indicated as white.

To exemplify the stochastic modeling, Figs 15(c) and (d) are shown, and they correspond to schemes of points A and B in Fig 15(b), respectively. The figures show the changes in modeled parameters (pressure, MFB, and Livengood-Wu integral) and the determined values following the previously suggested criterion. At point A, chosen Wiebe values for a and m for the model are 4.75 and 3.3, respectively. The individual heat release curve (red-indicated) can be derived from the representative curve by adopting the Wiebe values, and the black line in the figure indicates the modeled in-cylinder pressure calculated from it. The blue line curve is the Livengood-Wu integral using Eqs. 1 and 22 as a function of crank angle. The timing at which the Livengood-Wu integral reaches unity, i.e., predicted KO (blue open circle), was appeared at 7.3 CA aTDC prior to 7.8 CA aTDC of MFB85 (red circle); MFB85 is preceded by predicted KO, and this means knock will occur by the suggested criterion. Therefore, point A shows “Knock” on the binary map in Fig. 15(b). Likewise, Fig. 15(d) shows the point B case, and lower m value predominantly led to slower combustion speed which can be found in the lowered slope of MFB curve. Unlike the previous case, at point B, MFB85 is prior to the predicted KO so that the model considers such condition as a non-knocking condition as Fig. 15(b).

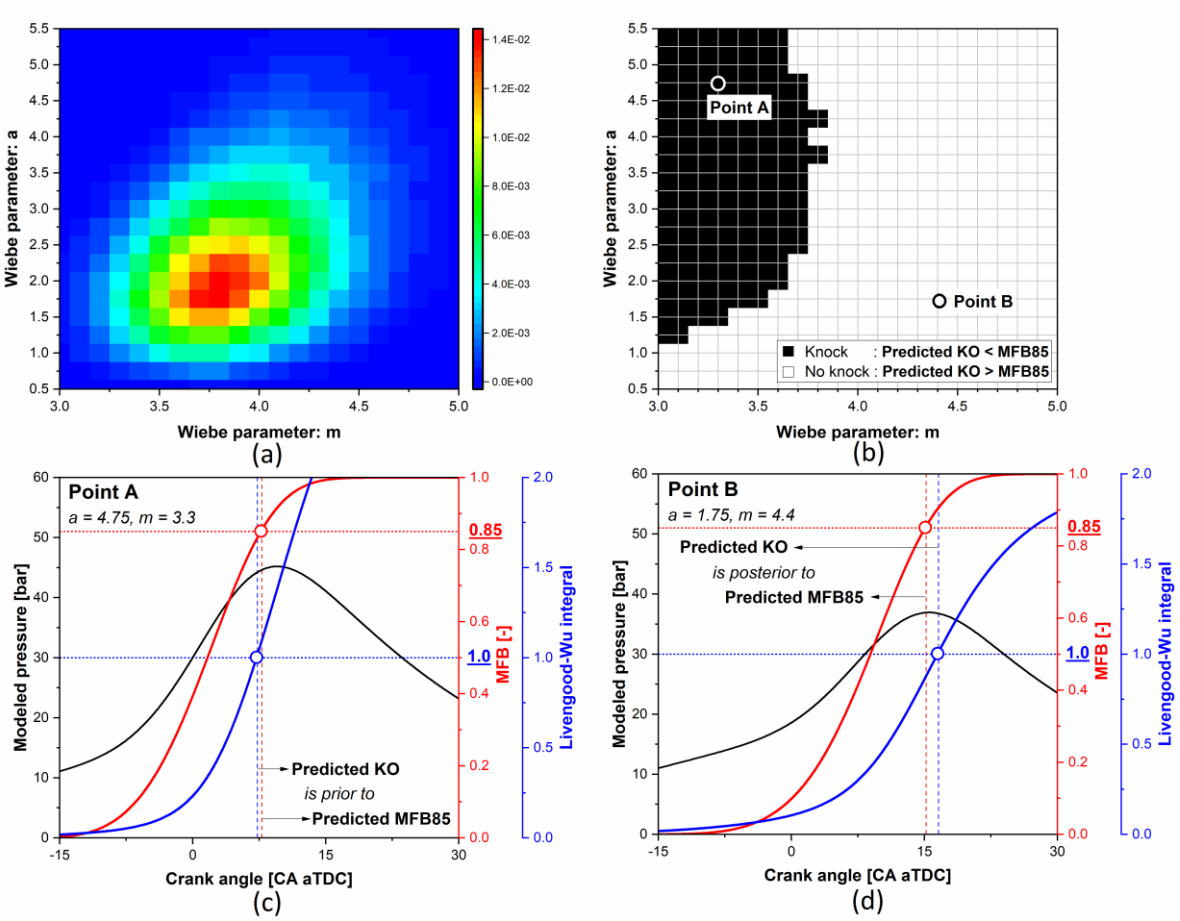

Fig. 15 Stochastic modeling of Wiebe parameters a and m; (a) 2D Probability density map (p_{ij}); (b) Binary map of knock occurrence (δ_{ij}); (c) Scheme example at point A with the modeled pressure, MFB and knock integral; (d) Scheme example at point B with modeled pressure, MFB and knock integral.

After that, the total sum of the simple multiplication of the 2D probability density (Fig. 15(a), p_{ij}) and binary value (Fig. 15(b), δ_{ij}) returns the probability of knock occurrence, i.e., the predicted knock incidence (the knock propensity at the given conditions) as shown in Eq. 23.

$$Modeled\ Knock\ Incidence\ = \sum_{i,j} p_{ij}\delta_{ij} \quad \text{(Eq. 23)}$$

Fig. 16 shows a parity plot comparing the prediction model results (y-axis) and experimental results (x-axis) associated with the knock incidence. Cases with zero knock incidence (< 1%) were excluded, so a total of 44 cases are presented. A satisfactory prediction model is achieved by all the prediction processes shown in Fig. 4, showing an R^2 value of 0.919. A poor correlation was found in the low knock incidence region that was less than 5%. Some reasons were the lower accuracy of the 0D RGF model and burn duration model. The discrepancy in both values entails a significant error in the prediction of in-cylinder pressure. In addition, the underestimation is also attributable to the fixed probability map of the Wiebe stochastic modeling. The map may need to be adjusted depending on the condition for better predictability in the future. However, the prediction values are still within the 15% error range, so it is concluded that the feasibility of the 0D model application was clearly shown.

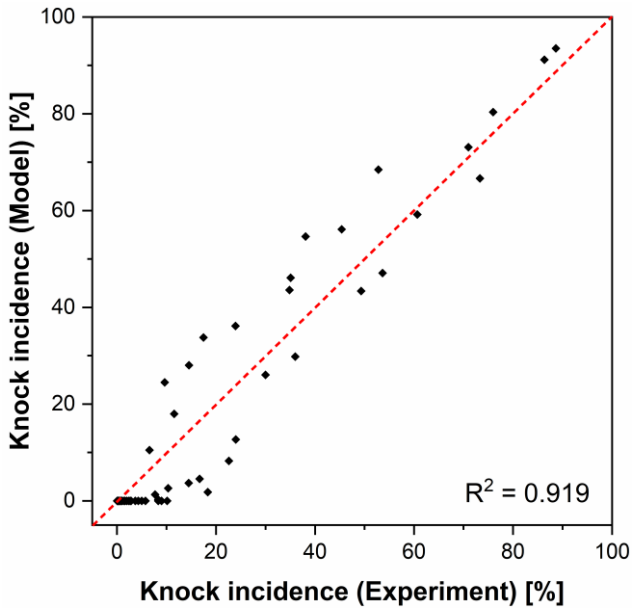

Fig. 16 Parity plot for validity of the developed prediction model for knock propensity.

There are still many sources from which the error originates. As discussed in this paper, the prediction process of the in-cylinder pressure can be improved using many other methods that could not be incorporated in this study. Also, it is essential to expand the proposed methodology to engines with external EGR, turbocharging, and direct injection as those technologies are actively adopted in production engines mainly by stringent emission regulations. In addition, as this study was conducted with a single-cylinder to study its feasibility, further studies considering cylinder-to-cylinder variations are needed. Likewise, finding a method to represent the cyclic variability [47] is also critical for accurate cyclic determination of the knock status. The ignition delay model can also be improved by adopting a two-stage ignition delay model to better represent the negative temperature coefficient behavior(s) of gasoline fuel and other potential fuels. It was found that the calculation load and speed of EMS are viable to predict the in-cylinder pressure and predict KO, and a similar study already proved it in a diesel engine [33]. However, further effort is required to minimize the load in the stochastic modeling process. The suggested models currently require calibration of the coefficients, which can easily be determined during the engine development process. However, the improvement of each model suggested above may eventually lead to the master model with better generality.

5. Conclusions

In this study, a novel modeling approach was developed for predicting the knock propensity in an SI engine. A methodology for pressure prediction was suggested, aiming to rely solely on EMS data rather than using other sensors, such as in-cylinder pressure transducers. The in-cylinder pressure at IVC timing (P_{IVC}) could be predicted with high accuracy (R^2 = 0.995) with the newly developed empirical model using a MAP sensor. Furthermore, the prediction model for the residual gas fraction was improved; therefore, the thermodynamic conditions of the closed system at IVC timing could be specified. The compression process (P_{IVC-ST}) was successfully modeled by assuming a polytropic process with a modified polytropic index, and the in-cylinder pressure during the combustion process (P_{IVC-ST}) was predicted using a representative heat release curve with sub-models for burn duration and

heat loss. Based on the predicted in-cylinder pressure, a 0D empirical correlation was applied with a pertinent criterion (MFB85) to predict KO and knock propensity (incidence). Stochastic modeling was introduced to finalize the calculation of knock incidence, and the Wiebe function parameters were chosen as perturbation factors. As a result, the predicted knock incidence showed a good match (R^2 of 0.92) with the values from the experimental results.

Although an incremental study is required to incorporate a wider engine operating range and different engine structures to secure a broader universality, the developed model showed remarkable feasibility and a general approach to predicting the knocking status of an engine. A virtual knock sensor which can support conventional knock sensors can be developed with the suggested methodologies, and an in-cylinder pressure transducer would no longer be needed for prediction, potentially leading to significant cost reductions in the field. In addition, there is potential for using such a model-based approach in engine combustion control systems utilizing autoignition, because the timing and unburned mass fraction can be known variables by the predictive model.

6. Acknowledgments

Research fellow Dr. Kyoung-pyo Ha and senior researchers Backsik Kim and Ingee Suh of the Hyundai Motor Company are gratefully acknowledged for their unconditional support in engine design and fabrication. Senior researcher Dr. Heechang Oh is greatly appreciated for providing insight during the research progress. Advanced Automotive Research Center (AARC) and Institute of Advanced Machinery and Design (IAMD) of Seoul National University are also thanked for supporting the research facility.

7. References

1. Heywood JB. *Internal Combustion Engine Fundamentals*. New York: McGraw-Hill, 1988.

2. Zhen X, Wang Y, Xu S, et al. The engine knock analysis–an overview. *Applied Energy* 2012; 92: 628-

636. DOI: http://doi.org/10.1016/j.apenergy.2011.11.079.

3. Wang Z, Liu H and Reitz RD. Knocking combustion in spark-ignition engines. *Progress in Energy and Combustion Science* 2017; 61: 78-112. DOI: https://doi.org/10.1016/j.pecs.2017.03.004.

4. Kaji K, Matsushige S, Kanamaru M, et al. Development of knock sensor. *SAE Technical Paper 861375* 1986: 315-323. DOI: https://doi.org/10.4271/861375.

5. Pla Bn, Bares P, Jiménez I, et al. A fuzzy logic map-based knock control for spark ignition engines. *Applied Energy* 2020; 280: 116036. DOI: https://doi.org/10.1016/j.apenergy.2020.116036.

6. Corrigan DJ, Breda S and Fontanesi S. A Simple CFD Model for Knocking Cylinder Pressure Data Interpretation: Part 1. *SAE Technical Paper 2021-24-0051*. 2021.

7. Cho S, Oh S, Song C, et al. Effects of Bore-to-Stroke Ratio on the Efficiency and Knock Characteristics in a Single-Cylinder GDI Engine. *SAE Technical Paper 2019-01-1138*. 2019.

8. Moriyoshi Y, Kuboyama T, Takaki T, et al. Investigation on Relationship between LSPI and Lube Oil Consumption and Its Countermeasure. *SAE Technical Paper 2021-01-0567*. 2021.

9. Vehicle Emissions On-Board Diagnostics (OBD), (accessed July 14, 2021).

10. Jones JCP, Spelina JM and Frey J. Likelihood-Based Control of Engine Knock. *IEEE Transactions on Control Systems Technology* 2013; 21: 2169-2180. DOI: http://doi.org/10.1109/TCST.2012.2229280.

11. Shen X and Shen T. Real-time statistical learning-based stochastic knock limit control for spark-ignition engines. *Applied Thermal Engineering* 2017; 127: 1518-1529. DOI: https://doi.org/10.1016/j.applthermaleng.2017.08.150.

12. Bares P, Selmanaj D, Guardiola C, et al. A new knock event definition for knock detection and control optimization. *Applied Thermal Engineering* 2018; 131: 80-88. DOI: https://doi.org/10.1016/j.applthermaleng.2017.11.138.

13. Livengood J and Wu P. Correlation of autoignition phenomena in internal combustion engines and rapid compression machines. *Symposium (international) on combustion*. Elsevier, 1955, p. 347-356.

14. Douaud A and Eyzat P. Four-Octane-Number Method for Predicting the Anti-Knock Behavior of Fuels and Engines. *SAE Technical Paper 780080*. 1978.

15. Wayne WS, Clark NN and Atkinson CM. Numerical Prediction of Knock in a Bi-Fuel Engine. *SAE Technical Paper 982533*. 1998.

16. Yates ADB and Viljoen CL. An Improved Empirical Model for Describing Auto-ignition. *SAE*

Technical Paper 2008-01-1629. SAE International, 2008.

17. Pipitone E and Beccari S. Calibration of a knock prediction model for the combustion of gasoline-natural gas mixtures. *ASME 2009 Internal Combustion Engine Division Fall Technical Conference*. American Society of Mechanical Engineers, 2009, p. 191-197.

18. Hoepke B, Jannsen S, Kasseris E, et al. EGR effects on boosted SI engine operation and knock integral correlation. *SAE International Journal of Engines* 2012; 5: 547-559. DOI: http://doi.org/10.4271/2012-01-0707.

19. Kasseris E and Heywood JB. Charge Cooling Effects on Knock Limits in SI DI Engines Using Gasoline/Ethanol Blends: Part 2-Effective Octane Numbers. *SAE International Journal of Fuels and Lubricants* 2012; 5: 844-854. DOI: https://doi.org/10.4271/2012-01-1284.

20. Chen L, Li T, Yin T, et al. A predictive model for knock onset in spark-ignition engines with cooled EGR. *Energy Conversion and Management* 2014; 87: 946-955. DOI: https://doi.org/10.1016/j.enconman.2014.08.002.

21. McKenzie J and Cheng WK. Ignition Delay Correlation for Engine Operating with Lean and with Rich Fuel-Air Mixtures. *SAE Technical Paper 2016-01-0699*. 2016.

22. Cho S, Park J, Song C, et al. Prediction Modeling and Analysis of Knocking Combustion using an Improved 0D RGF Model and Supervised Deep Learning. *Energies* 2019; 12: 844. DOI: http://doi.org/10.3390/en12050844.

23. Yue Z, Xu C, Som S, et al. A Transported Livengood–Wu Integral Model for Knock Prediction in Computational Fluid Dynamics Simulation. *Journal of Engineering for Gas Turbines and Power* 2021; 143. DOI: https://doi.org/10.1115/1.4050583.

24. Sazhin S, Sazhina E, Heikal M, et al. The Shell autoignition model: a new mathematical formulation. *Combustion and flame* 1999; 117: 529-540. DOI: https://doi.org/10.1016/S0010-2180(98)00072-8.

25. Sazhina E, Sazhin S, Heikal M, et al. The Shell autoignition model: applications to gasoline and diesel fuels. *Fuel* 1999; 78: 389-401. DOI: https://doi.org/10.1016/S0016-2361(98)00167-7.

26. Leppard WR. A detailed chemical kinetics simulation of engine knock. *Combustion Science Technology* 1985; 43: 1-20. DOI: https://doi.org/10.1080/00102208508946993.

27. Cowart JS, Keck JC, Heywood JB, et al. Engine knock predictions using a fully-detailed and a reduced chemical kinetic mechanism. *Symposium (International) on Combustion* 1991; 23: 1055-1062. DOI: https://doi.org/10.1016/S0082-0784(06)80364-4.

28. Ma J, Kwak KH, Lee B, et al. An empirical modeling approach for the ignition delay of fuel blends based on the molar fractions of fuel components. *Fuel* 2016; 164: 305-313. DOI:

https://doi.org/10.1016/j.fuel.2015.09.069.

29. Fandakov A, Grill M, Bargende M, et al. Two-stage ignition occurrence in the end gas and modeling its influence on engine knock. *SAE International Journal of Engines* 2017; 10: 2109-2128. DOI: https://doi.org/10.4271/2018-01-0855.

30. Song H and Song HH. Correlated ignition delay expression of two-stage ignition fuels for Livengood-Wu model-based knock prediction. *Fuel* 2020; 260: 116404. DOI: https://doi.org/10.1016/j.fuel.2019.116404.

31. Lee Y and Min K. Estimation of the Polytropic Index for In-cylinder Pressure Prediction in Engines. *Applied Thermal Engineering* 2019. DOI: http://doi.org/10.1016/j.applthermaleng.2019.04.113.

32. Lee Y, Lee S and Min K. Semi-empirical estimation model of in-cylinder pressure for compression ignition engines. *Proceedings of the Institution of Mechanical Engineers, Part D: Journal of Automobile Engineering* 2020; 234: 2862-2877. DOI: https://doi.org/10.1177/0954407020916952.

33. Lee Y, Lee S, Han K, et al. Prediction of In-Cylinder Pressure for Light-Duty Diesel Engines. *SAE Technical Paper 2019-01-0943*. 2019.

34. Li RC, Zhu GG and Men Y. A two-zone reaction-based combustion model for a spark-ignition engine. *International Journal of Engine Research* 2021; 22: 109-124. DOI: https://doi.org/10.1177/1468087419841746.

35. Li RC and Zhu GG. Model-based Knock Prediction and its Stochastic Feedforward Compensation. *2020 IEEE/ASME International Conference on Advanced Intelligent Mechatronics (AIM)*. 2020, p. 637-642.

36. Cho S, Song C, Kim N, et al. Influence of the wall temperatures of the combustion chamber and intake ports on the charge temperature and knock characteristics in a spark-ignited engine. *Applied Thermal Engineering* 2021; 182: 116000. DOI: https://doi.org/10.1016/j.applthermaleng.2020.116000.

37. Brunt MF, Pond CR and Biundo J. Gasoline Engine Knock Analysis using Cylinder Pressure Data. *SAE Technical Paper 980896*. 1998.

38. Eriksson L and Andersson I. An Analytic Model for Cylinder Pressure in a Four Stroke SI Engine. *SAE Technical Paper 2002-01-0371*. 2002.

39. Fox JW, Cheng WK and Heywood JB. A Model for Predicting Residual Gas Fraction in Spark-Ignition Engines. *SAE Technical Paper 931025*. 1993.

40. Kale V, Yeliana Y, Worm J, et al. Development of an Improved Residuals Estimation Model for Dual Independent Cam Phasing Spark-Ignition Engines. *SAE Technical Paper 2013-01-0312*. 2013.

41. Woschni G. A Universally Applicable Equation for the Instantaneous Heat Transfer Coefficient in the Internal Combustion Engine. *SAE Technical Paper 670931*. 1967.

42. Kim KS. *Study of engine knock using a Monte Carlo method*. The University of Wisconsin-Madison, 2015.

43. Bonatesta F, Waters B and Shayler PJ. Burn angles and form factors for Wiebe function fits to mass fraction burned curves of a spark ignition engine with variable valve timing. *International Journal of Engine Research* 2010; 11: 177-186. DOI: http://doi.org/10.1243/14680874jer05009.

44. Kalghatgi G, Morganti K, Algunaibet I, et al. Knock prediction using a simple model for ignition delay. *SAE Technical Paper 2016-01-0702*. 2016.

45. Foong TM, Brear MJ, Morganti KJ, et al. Modeling End-Gas Autoignition of Ethanol/Gasoline Surrogate Blends in the Cooperative Fuel Research Engine. *Energy & Fuels* 2017; 31: 2378-2389. DOI: https://doi.org/10.1021/acs.energyfuels.6b02380.

46. Kim N, Vuilleumier D, Sjöberg M, et al. Using Chemical Kinetics to Understand Effects of Fuel Type and Compression Ratio on Knock-Mitigation Effectiveness of Various EGR Constituents. *SAE Technical Paper 2019-01-1140*. 2019.

47. Moriyoshi Y, Kamimoto T, and Yagita M, Prediction of Cycle-to-Cycle Variation of In-cylinder Flow in a Motored Engine. *SAE Technical Paper 930066. 1993.*